Nuclear Inst. and Methods in Physics Research, A 1001 (2021) 165247

Contents lists available at ScienceDirect

Nuclear Inst. and Methods in Physics Research, A

journal homepage: www.elsevier.com/locate/nima

Multimodal simulation of large area silicon photomultipliers for time resolution optimization

David Sánchez [a,*], Sergio Gómez [a], José María Fernández-Tenllado [a,b], Rafael Ballabriga [b], Michael Campbell [b], David Gascón [a]

[a] Institute of Cosmos Science from University of Barcelona (ICC-UB), Martí i Franqués 1, Barcelona 08028, Spain
[b] CERN, 1211 Geneva 23, Switzerland

ARTICLE INFO

Keywords:
ASIC
Fast timing
Medical imaging
Front-end electronics
Silicon photomultiplier
Simulation

ABSTRACT

The Silicon Photomultiplier (SiPM) sensor is replacing the extensive use of the Photomultiplier Tube (PMT) in fast timing applications. These photo-sensors can be applied in different fields such as medical imaging systems like Positron Emission Tomography (PET), LIDAR technologies or High Energy Physics (HEP) experiments. More specific, Time-of-Flight PET (ToF-PET) requires further developments to achieve a Coincidence Time Resolution (CTR) of 10ps, this enabling the real time reconstruction and in vivo molecular examination. The most recent state-of-the-art ToF-PET systems can reach 200 ps in CTR. Lowering this value will require a cross-optimization of the scintillator crystal, the sensor and the electronics at the same time. These three elements optimization will be the key to boost the timing resolution of the complete system. The aim of this work is to provide a simulation framework that enables this cross-optimization of the PET system taking into consideration the photon physics interaction in the scintillator crystal, the sensor response (size, dead area, capacitance) and the readout electronics behavior (input impedance, noise, bandwidth). This framework has allowed us to study a new promising approach that helps reducing the CTR parameter by segmenting a large area SiPM into "m" smaller SiPMs and then, summing the signals to recover all the signal spread along these smaller sensors. A 15% improvement on time resolution is expected by segmenting a 4 mm × 4 mm single sensor into 9 sensors of 1.3 mm × 1.3 mm with respect to the case where no segmentation is applied.

1. Introduction

The Silicon Photomultiplier (SiPM) sensor is replacing the extensive use of the Photomultiplier Tube (PMT) in many applications. Nowadays, medical imaging systems such as Single Photon Emission Computed Tomography (SPECT) and Positron Emission Tomography (PET) are mainly running those new SiPMs. Moreover, most of the new upgrades in High Energy Physics (HEP) experiments are planning to use SiPMs [1], as well as for Cherenkov light detection [2–5], cosmic ray and space exploration detectors such as HERD [6] and LIDAR applications in automotive [7,8].

An application where the usage of SiPMs provides a noticeable performance improvement is medical imaging, in particular PET. PET is a molecular diagnosis technique that allows to track different biological processes, whose purpose is to show the cellular or molecular activity of the disease [9].

One approach to increase the sensitivity of the PET technique, thus reducing the dose to the patient or the scanning time, consist in pushing the limits of the ToF capabilities [10] by improving the CTR parameter of the system. This will have a direct impact on the image Signal-to-Noise (SNR), resulting in an improvement of the sensitivity by a theoretical factor of (Eq. (1)):

$$SNR_{ToF}/SNR_{NONToF} = \sqrt{\frac{2D}{c \cdot CTR}} \quad (1)$$

where D is the diameter of the Field of View (FoV) and c corresponds to the speed of light.

The latest developments on ToF-PET imaging systems have achieved a CTR of 200 ps as shown in the Biograph Vision model from Siemens Healthineers [11]. In fact, this value corresponds to an improvement factor of 1.5 with respect to the previous version and to the rest of existing systems that have a time resolution between 300 ps to 400 ps for partial or total body PET systems [12].

Different research groups are trying to break the barrier on time resolution and reach a CTR of 10 ps [13]. As a result, it will bring obvious societal and economic benefits, such as screening and early diagnosis of cancer, cardiovascular and degenerative diseases [14].

The basic PET module is composed by: first, a scintillator crystal that converts the gamma ray into visible light. Second, a photo-sensor

* Corresponding author.
E-mail address: dsanchez@fqa.ub.edu (D. Sánchez).

https://doi.org/10.1016/j.nima.2021.165247
Received 14 August 2020; Received in revised form 11 March 2021; Accepted 11 March 2021
Available online 21 March 2021

which collects the optical photons and outputs an electrical signal. Lastly, a dedicated electronics that processes this signal and generates readable data that will be used to generate the final image from the patient. Fig. 1 illustrates the detector module.

Nowadays, SiPMs are outperforming PMTs in all ToF-PET medical devices due to the astonishing improvements during the last 10 years. The silicon solid state detector is insensitive to magnetic fields, operates at low voltage compared to a PMT (20 V to 60 V) and it has excellent timing performance [16]. Moreover, the scalability and cost effectiveness makes them suitable for covering large detection area. The accuracy of the SiPM in determining the time of arrival of a single photon is referred to Single Photon Time Resolution (SPTR) [16]. The SPTR of the SiPM is one of the key factors that affects the CTR, but there are several other sources that affect the time jitter during the detection chain as shown in Fig. 1 [15].

We can separate the contributions to the time jitter as:

- **Scintillator crystal**: it is the responsible of three contributions on the time jitter. First, the fluctuation on the interaction depth of the gamma photon (t_{depth}), which follows an exponential attenuation with the maximum at the entrance face. Then, the scintillator process determines the emission time of each one of the optical photons ($t_{scint.}$). Finally, the Transit Time Spread (TTS) which is the time needed for the optical photon to reach the photosensor (t_{TTS}) and it depends on the photon travel path. An optical coupler with a refractive index between the scintillator crystal and the SiPM window is used to increase the photon extraction such as Meltmount 1.582 or BC 631 from Saint-Gobain.
- **SiPM**: The avalanche process inside the solid state detector along with the Photo-Detection Efficiency (PDE) is the main factor involved in the photon absorption [17]. Nowadays, the PDE has increased to almost 60 % [18], which means that the number of photons detected has to be multiplied by 0.6 with respect to the total extracted photons as a first approximation. Additionally, the avalanche process is a stochastic phenomena which implies that the trigger timestamps will vary among different avalanche events. This affects the time jitter at a single photon level (t_{SPTR}).
- **Electronics**: the analog signal generated from the SiPM is processed by a Front-End (FE) electronics and a Time to Digital Converter (TDC) that picks up the time of arrival (ToA) of the photons. Both circuits introduce time fluctuations to capture the ToA due to the electronic noise and therefore a time jitter that is represented as $t_{elec.}$ taking into account both contributions, the Front-End readout and the TDC time uncertainty.

The aim of this work is twofold. Firstly, to show a novel framework that will enable the optimization of a PET module, including the sensor, scintillator crystal and electronics. Secondly, using this framework, the time jitter of the current systems can be investigated by using the segmentation approach, where a single sensor is subdivided in smaller sensors and the individual signals summed as a single output.

Although this framework is here employed for ToF-PET time optimization, it is suitable for any application where the same detector module is required, as depicted in Fig. 1. High energy physics and any experiment involving optical photon collection and time resolution optimization are eligible to use it.

The following sections are organized as follows. Section 2 details how the complete framework works, starting by the physics simulator description and followed by the electrical simulator here used. Then, Section 3 shows the theoretical approach on sensor segmentation and their impact on time performance. Afterwards, the simulation results for SPTR and CTR will be shown in Sections 4 and 5 respectively. Finally, the conclusions and future work regarding the use of the framework are described in Section 6.

2. Simulation framework

This section will present the simulation environment created to study and optimize the time jitter from the point of view of the photodetector and the electronics readout. First, we will explain how GATE, the physics simulator, tracks the detected photons and generates a readable output. Then, the next section will be focused on the electrical simulator used in this work, without loss of generality, Spectre simulator from Cadence Design Systems [19], and how this tool uses the information from GATE to compute the detector and electronics readout response.

2.1. Optical photon transport simulation: GATE

GATE is an advanced open-source software developed by the international collaboration OpenGATE [20] and dedicated to numerical simulations in medical imaging and radiotherapy based on GEANT4. Accurate modeling of photon interactions with crystal surfaces is essential in optical simulations, but the existing UNIFIED model in GATE is often inaccurate, especially for rough surfaces.

A new approach was developed for GATE, named Davis Model [21]. This method calculates the reflectance properties from the crystal topography previously measured with either an atomic force microscope (AFM) or a confocal laser scanning microscopy (CLSM). Fig. 2 illustrates a small region from one of our scanned scintillator crystal surface using a CLSM. The data collected in this process are stored in a Look-Up-Table (LUT), and then used during the simulation to predict the photon direction after impinging into a crystal surface. This feature makes GATE a strong photon transport Monte Carlo generator that will be used to simulate the first steps in a gamma collection process, involving the gamma conversion into optical photons and their collection by the photo-sensor.

First, we define a CTR setup consisting of: a ^{22}Na point source in between two scintillator crystals of tunable length, both crystal surfaces wrapped in teflon if nothing different specified. Interface surfaces are defined accordingly to the DAVIS model parameters. As previously mentioned, we can generate our own DAVIS LUT from a prior scanned crystal surface using an AFM or CLSM. These crystals are coupled to a sensor with matching cross-sections by using an intermediate layer of optical grease, whose optical properties, such as the refraction index, can be adjusted in the simulation. The sensor PDE spectrum from the datasheet of the manufacturer can be introduced as a parameter in the simulator. Fig. 3 illustrates the typical CTR setup described in a GATE simulation.

The full process starts by the emission of a positron from the ^{22}Na radioactive source which annihilates with an electron, resulting in two back-to-back 511 keV gamma photons. Each one of them interacts with the crystal depending on the physics interaction (Compton scattering or Photoelectric effect). Then, a certain number of photons are generated according to the light yield of the scintillating crystal. A fraction of those will reach the sensor at a given time depending on the travel path inside de crystal.

The root file output from GATE simulation includes the arrival times of each one of the scintillator photons, as well as the impact position on the sensor surface. Then, we prepare the data using a Python-root script that takes the raw file and generates a suitable output file to be used in a specific electrical simulator. Only photons with an specific arrival time below a certain threshold are selected. This threshold represents the maximum arrival time of the detected photons to be considered on the output file, any photon above this threshold will be discarded. Hence, reducing the simulation time consumption, whereas maintaining the performance due to the fact that only a few tens of photons are needed to reconstruct the rising edge of the analog signal from the SiPM. This data simplification is only allowed for a leading edge discriminator time pick-up approach that does not need the peak amplitude of the SiPM to extract the arrival time. For instance,

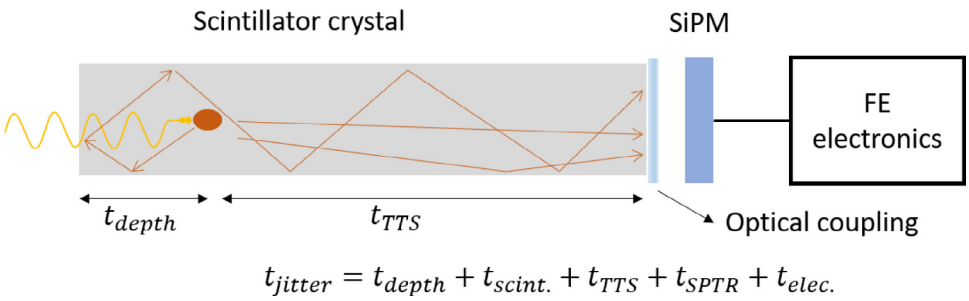

Fig. 1. Time jitter contributions in the gamma photon detection chain from crystal, SiPM and electronics. *Source:* Modified image from [15].

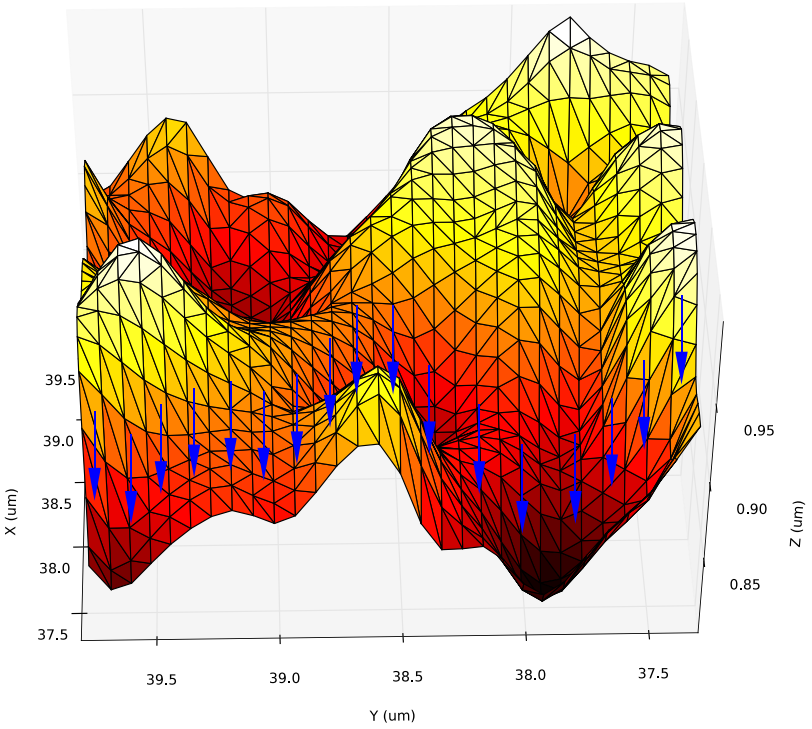

Fig. 2. 3D Surface representation and photon ray-tracing along different impact points (blue arrows). The resulting reflected and transmitted directions are stored in a LUT.

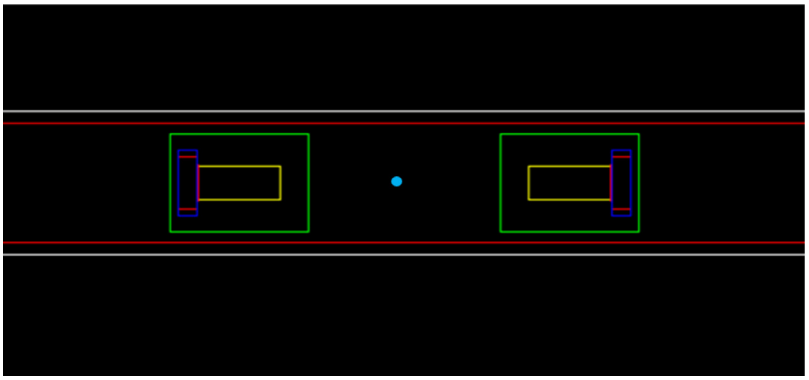

Fig. 3. CTR setup screenshot from GATE simulator. In Cyan, the ^{22}Na source between detectors and in green, the whole detector module. Inside the green box in yellow, the scintillator crystal and in red, the SiPM detector and the optical grease. (For interpretation of the references to color in this figure legend, the reader is referred to the web version of this article.)

a Constant Fraction Discriminator (CFD) or any other amplitude signal dependent method cannot apply this photon prune, since they need the amplitude to obtain the arrival time. In addition, the SiPM channel characteristics such as active area or micro-cell size can be taken into account within the input parameters in the script. The cell size limits the number of photons collected, due to the fact that there is a dead time between two consecutive photons arriving on the same cell. Thus, losing photon detection at high light rates.

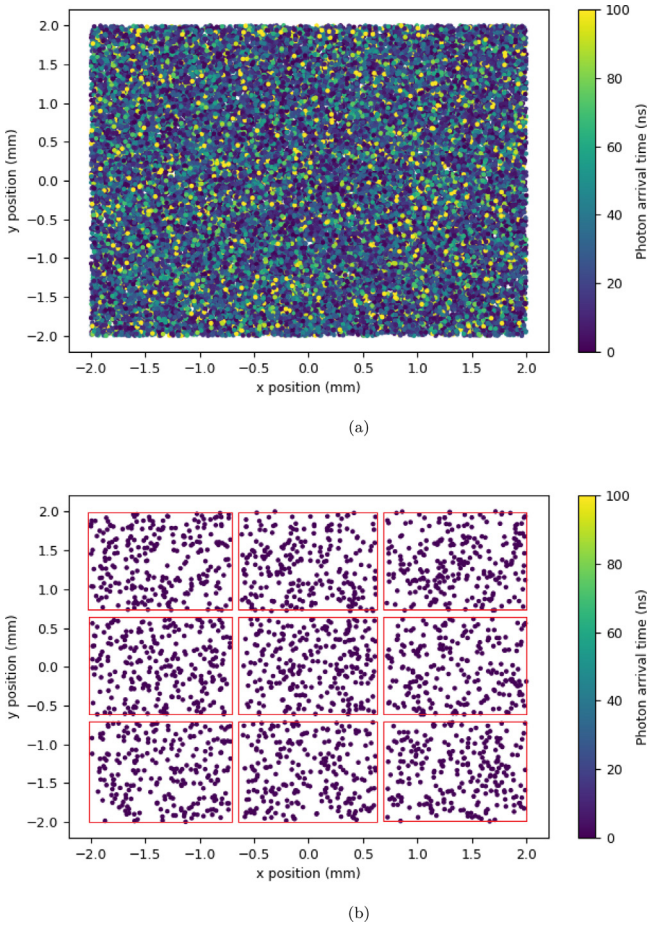

Fig. 4. Photon impact position and arrival time at the SiPM surface: (a) before cleaning the data. (b) after applying all constrains referring to SiPM channel, cell size and arrival time threshold.

Fig. 4 shows the photon impact distribution as well as the associated arrival time ($t_{arrival}$). In this example, we set a total of 9 SiPM channels (red boxes) with 50 μm × 50 μm cell size, 0.1 mm of dead space between channels (blank space between one channel and the neighbor), as depicted in Fig. 4(b), and 1 nanosecond threshold on the arrival time. The scintillator crystal is a LYSO of 4 mm × 4 mm × 10 mm and the SiPM employed is the S14160-4050HS from Hamamatsu at 5 V of overvoltage. The output file will contain the remaining photons after all the pruning process. Additionally, the intrinsic t_{SPTR} is added right after the pruning. In this stage, a random timestamp generated by a Gaussian distribution is summed to the actual arrival time of the photon. The sigma of this Gaussian is directly the intrinsic SPTR of the modeled SiPM sensor. Thus, the contribution of the t_{SPTR} can be obtained using the following expression:

$$t_{SPTR} = \frac{1}{\sigma_{SPTR}\sqrt{2\pi}} exp\left[-\frac{t^2}{2\sigma^2_{SPTR}}\right] \quad (2)$$

For instance, the SiPM S14160-4050HS has a SPTR of 50 ps [18] in sigma. Combining the associated arrival time with the contribution of the SPTR, gives a final timestamp defined as:

$$timestamp_{final} = t_{arrival} + t_{SPTR} \quad (3)$$

The final timestamp of the selected photons is used as input in the electrical simulator to emulate the response of the SiPM [22]. Next section, shows how the time information from the optical simulation is combined with the electrical response of the front-electronics.

2.2. SiPM signal generation

The SiPM is a semiconductor photodiode build of many Single Photon Avalanche Detectors (SPADs) or microcells joint together on silicon substrate with common load. Typically in SiPMs, the microcells are of identical size and arranged in a rectangular pattern. Depending on the device, the size of a microcell varies from 10 μm to 100 μm and the number of microcells per device ranges from several hundreds to several tens of thousands, depending on the active area. The SiPM schematic circuit is modeled in the electronic simulator following the model detailed in [23]. A equivalent circuit of the SiPM electrical model can be seen in Fig. 5 [24].

Regarding the electrical simulation using this equivalent circuit, in this work we used Cadence Design environment with the Spectre simulator [19]. This toolkit enables the possibility to simulate the electrical response of the SiPM in combination with the arrival time of the photons and a dedicated Front-End electronics for its signal processing. Nonetheless, any other electrical simulators capable of introducing transient noise on the time domain could be adapted to work with the same input file.

The equivalent SiPM electrical circuit simulating the discharge of the cells works as follows. Before any photon detection, the switch S_A is opened and the detector capacitance (C_d) is charged to the SiPM bias voltage (V_{bias}) applied between the anode and cathode. When a photon arrives to the SiPM (using the timestamp of each photon from GATE's output file), this switch closes making the start of a breakdown event (N_f corresponds to the number of cells fired). We can control S_A closing time through a veriloga code that closes it as a function of the photon arrival time. At this moment, the avalanche begins, C_d capacitance discharges through R_d ($R_d \ll R_q$) with the rising time constant $R_d(C_d + C_q)$. The discharge is stopped when the voltage across V_{bd} and R_d drops below a predefined threshold quenching current I_q [23] and thus quenching the avalanche. The external polysilicon resistor (R_q) decouples electrically each cell and limits the current drawn by the diode during breakdown.

Once the avalanche is quenched and switch S_A is opened, V_{bias} recharges C_d with an exponential process with two time constants [24, 25]. The first time constant is attributed to the fast supply path across C_d and the capacitive coupling through the parasitic quenching capacitance C_q with a fast time constant of $R_{load}C_{tot}$, where the overall capacitance C_{tot} is $C_g + N_{tot}(C_d + C_q)$ and the R_{load} is associated to the input impedance of the FE electronics. The second time constant, the slow component, is due to the exponentially decreasing recharge current flowing through the quenching resistor R_q. The slow component, known as the SiPM recovery time constant since dominates the tail of the response, is determined by $R_q(C_d + C_q)$ and it is in the order of tens to hundreds of nanoseconds. Recharge of the SiPM ends when V_D reaches V_{bias}.

The intrinsic parameters of the SiPM are extracted using the following procedure. Experimentally each sensor is tested using a large bandwidth and low noise pre-amplifier (PACTA pre-amplifier [26]) to better capture the response of the SiPM. In this scenario, a picosecond pulsed laser (PiLas Picosecond Diode Laser at 405 nm, 30 ps pulse width) sends a photon pulse to the SiPM through a single mode fiber and a Liquid Crystal Optical Beam Attenuator from Thorlabs. The optical photons are then converted into an small electrical current by the SiPM and the pulse is amplified by the PACTA chips, which is then recorded by an Agilent MSO9404 A Mixed Signal oscilloscope 4 GHz (20 Gsa/s). An extended explanation on how to characterize a photodetector can be found in [27], while Fig. 6 illustrates the setup involved during the waveform acquisition.

$C_d + C_q$ was determined via the SiPM gain. Additionally, the signal shape of the first photon is acquired. Lastly, the R_q is obtained via the forward I–V characteristic curve. Then, using the SiPM (Fig. 5) and the PACTA electrical model with RC parasitics on the simulation environment (Cadence [19]), we can adjust the other parameters

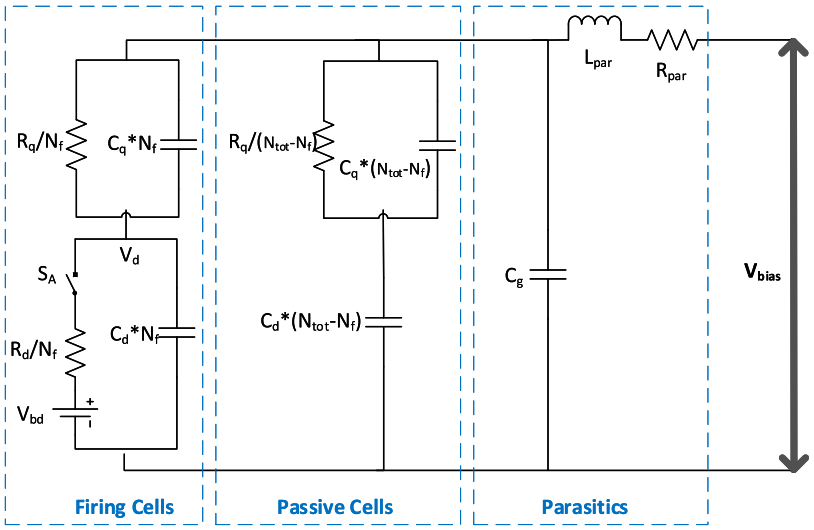

Fig. 5. Schematic representation of the SiPM model.

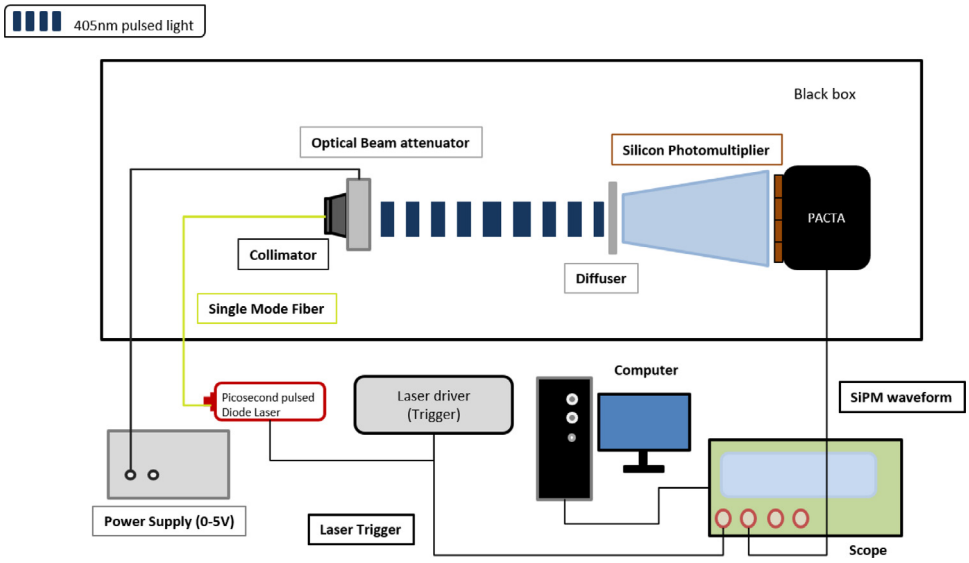

Fig. 6. Characterization setup using a picosecond pulsed laser.

(R_d, C_d, C_q and C_g) by matching the simulated response with the pulse shape acquired in the measurements. In this process, the values for R_q and $C_d + C_q$ are taken from the previous characterization. Besides of adjusting the shape of the real data and the signal from the simulation, the SiPM gain in Eq. (4) must be as close as possible in order to guarantee an accurate simulation model to extract the parameters of the SiPM.

$$SiPM_{gain} = \frac{Q}{q} \tag{4}$$

where is Q the total charge from the single photon response and q is the electron charge.

An example of the resultant SiPM voltage waveform generated from 1 cell fired along with the simulated model can be seen in Fig. 7. Having a good and reliable model of all those parameters is critical for the time resolution optimization of the system. Note that the correlated and non-correlated noise, those including dark counts (DCR), cross-talk and after-pulsing, are not taken into account in this work. Future updates on the simulation framework will implement both of them.

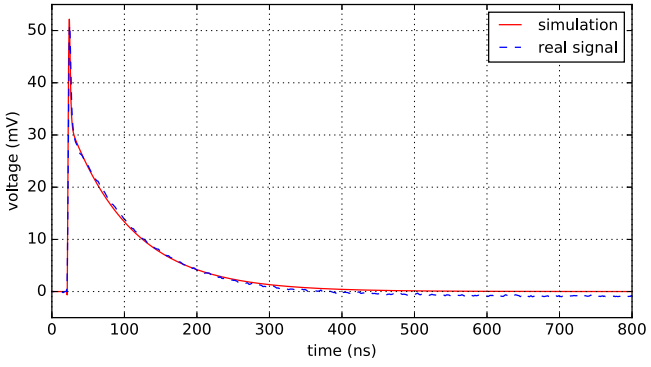

Fig. 7. SiPM signal waveform comparison between the simulated model and the real output for 1 fired cell acquired in the test bench using a FBK NUV-HD model of 4 mm × 4 mm readout by the PACTA preamplifier chip.

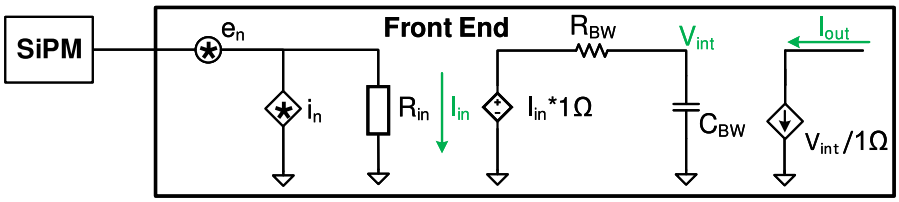

Fig. 8. Front end schematic representation used in the electrical simulator.

2.3. FE electronics

The output of the SiPM can be connected to a FE readout circuit to evaluate the time response of the overall system (scintillator, sensor and electronics). This framework can be employed with the complete FE electronics, part of it affecting to the time response or even with a simplified equivalent circuit of the readout electronics. Fig. 8 shows a parameterized FE circuit which enables the possibility to study the impact on time resolution using a simplified model. In this case, a current sensing FE model has been employed, but a similar FE structure can be used for a voltage sensing. This FE has the following parameters: an input impedance represented as R_{in}, an equivalent input series noise voltage (e_n) and an equivalent input parallel noise voltage (i_n) as the two noise sources present on the FE. The parasitic inductance between the SiPM and the FE is represented by L_{par}. Additionally, the parameters R_{BW} and C_{BW} are related to the bandwidth limitation of the system by the following equation:

$$BW = \frac{1}{2\pi C_{BW} R_{BW}} \tag{5}$$

This simplified model that emulates the response of the readout circuit, enables to study different configurations of the FE electronics depending on the sensor employed. The simplified circuit makes the electrical simulation much faster than employing a full FE chips and thus different crystals, sensors and internal parameters can be optimized. Lastly, the time uncertainty introduced by the electronics is simulated with Cadence Design by performing a transient noise simulation [28]. This analysis takes into account the noise sources of the electrical circuit and performs a simulation in the time domain to emulate the response of the complete system. Therefore, the time uncertainty or the jitter component of the electronics can be also taken into account in the overall response of the system.

Concluding, this framework permits to find an optimal configuration of the FE electronics for a given sensor (with its respective internal parameters). Moreover, it also permits to study the impact on changing some parameters of the sensor, such as C_q or R_q, on the timing response of the overall system.

2.4. Framework validation

To have a broad overview of the framework, a general explanation on how it works can be read as follows: first, each SiPM channel generates an analog signal according to the number of photons and arrival time described in GATE's output file and the impulse response (single photon signal) obtained as described in Sections 2.1 and 2.2. Then, each signal is processed by an specific FE readout. This FE is basically composed by a pre-amplifier analog readout circuit to capture the response of the sensor and a discriminator, e.g., a leading-edge comparator, to provide the arrival time of the photons. Lastly, a transient noise simulation is performed to emulate the response of complete system. Note that the CTR is obtained as the standard deviation of the cumulative delay distribution from the time response of the two detectors. In brief, this electrical simulator allows to generate and process the signal from the SiPM in combination with the arrival time information from the photons simulated in GATE. Or in other words, this framework comprehends the whole physics involved in the fast timing optimization for PET application.

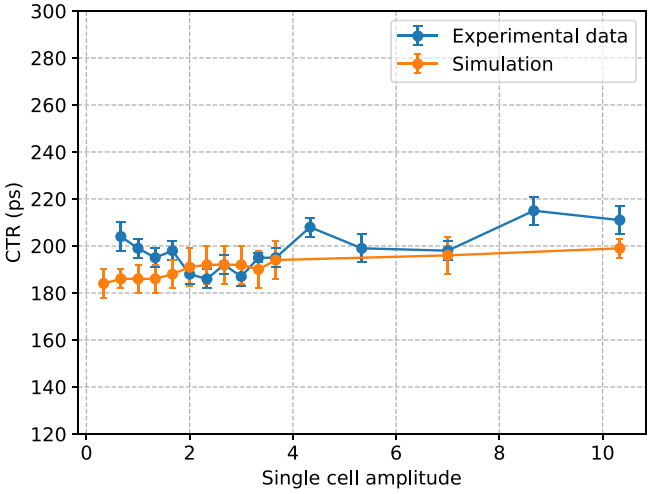

Fig. 9. Simulation results and laboratory measurements comparison. CTR in FWHM.

We compared real CTR data from a well known setup and the simulation results obtained from the new GATE + Cadence environment. This setup was composed by: Lutetium Fine Silicate (LFS) scintillator crystals of 3 mm × 3 mm × 20 mm size, coupled to the SiPM of 3 mm × 3 mm and 50 μm × 50 μm micro-cell size, readout by a real FE electronics from an ASIC named HRFlexToT described in [29]. This ASIC provides the arrival time of the photons by using a low input impedance current conveyor and a leading-edge discriminator. Thus, we compared simulation results obtained using the framework with the HRFlexToT circuit with respect to direct measurements employing the same ASIC.

Figs. 9 shows good agreement with the laboratory measurements. The trend of the CTR values as a function of the threshold are close between the simulated and experimental results, besides the first data points (0–2 firing cells), because of the intrinsic DCR noise which is not being simulated in the current scenario as previously mentioned. This result gives a trusting simulation tool to proceed with further and more complex scenarios, as shown in the next sections.

3. SiPM segmentation approach

SiPM suffers various inconveniences when increasing the area of the detector. The main effect comes from the intrinsic capacitance (equivalent capacitance at high frequency of a single cell [22,24,30]), which is a few orders of magnitude larger compared to the capacitance of a PMT, and additionally, it scales with the active area. This increase of the capacitance with the area changes the rising time of the SiPM electrical signal as the peak amplitude is proportional to C^{-1} [25]. Hence, a large SiPM also implies that the slew rate (SR) decreases with respect to a smaller SiPM (Fig. 10), thus worsening the timing properties on "fast" applications such as ToF-PET. Eq. (6) details how the jitter or SPTR is being affected by the SR at a specific threshold and the integrated output noise (σ_n).

$$\sigma_{telec.} = \frac{\sigma_n}{SR_{thr}} = \frac{\sigma_n}{(\partial I_{o1p}/\partial t)_{thr}} \tag{6}$$

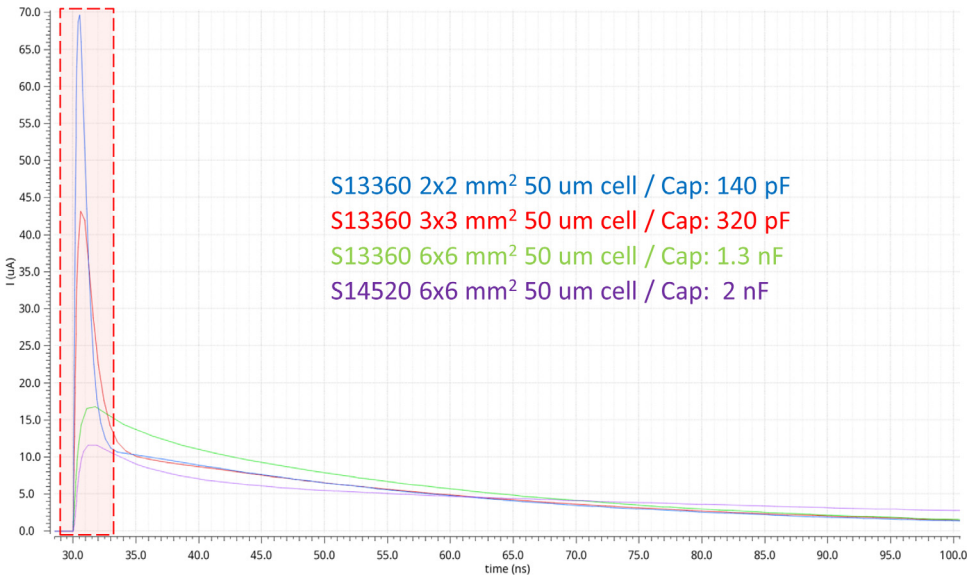

Fig. 10. Simulated single cell signal for different SiPM area. Observe the red region (beginning of the signal) where the peak amplitude and the SR of the signal increases when the capacitance decreases.

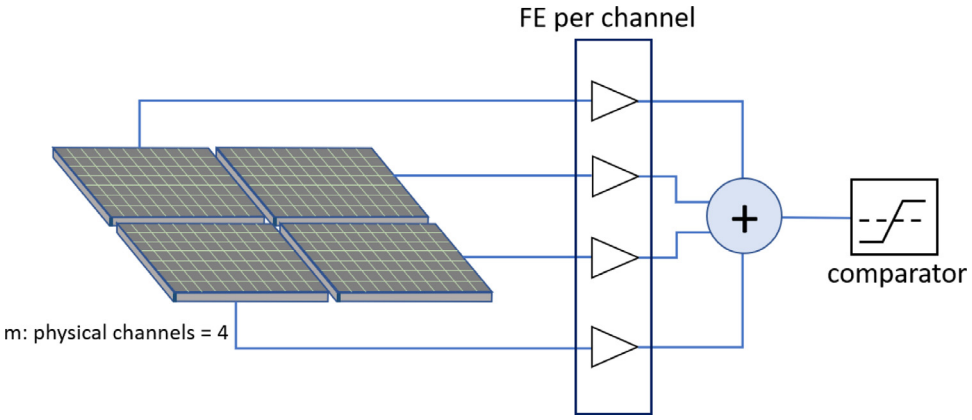

Fig. 11. Segmentation and analog summation scheme.

∂I_{o1p} corresponds to the output current for the signal of 1 photon (1 cell fired).

Front End electronics coupled to large area SiPMs presents smaller slew rate and higher output noise, making $\sigma_{telec.}$ increase and therefore, degrading the time performance [31]. Nevertheless, the cumulative charge of the signal is constant with the capacitance but, as the capacitance increases, the integration time needed to recover the same charge is also larger and thus reducing the SNR.

Segmenting a large area sensor into "m" smaller ones will help dealing with the problem of high intrinsic capacitance (at expense of increasing the power consumption). Hence, we would take advantage of the increase in slew rate of a small area SiPM and then, all analog signals will be summed up to recover the single signal output covering the same area. Fig. 11 shows the schematic representation of the SiPM of area A divided in 4 smaller SiPMs with individual area of $A/4$, which implies 4 times smaller capacitance. The analog signal of each small sensor is read out by a dedicated FE circuit and then summed, i.e., using an ideal summation for this study. Finally, using a leading-edge comparator, in this case an ideal ToT, the time of arrival is obtained.

On one side, previous work from S. Deker, et al. [32] studied the CTR performance of a 6 mm × 6 mm × 20 mm readout by 3 levels of SiPM segmentation: 1 SiPM of 6 mm × 6 mm, 4 SiPMs of 3 mm × 3 mm and 9 SiPMs of 2 mm × 2 mm. In each case, the individual sensor was readout by a NINO ASIC channel [33]. If more than one channel were used, the timestamp of each channel was combined using weighted average methods and applying time walk and time skew corrections, similar to what is traditionally done in monolithic crystals. In this case, besides the improvement in noise achieved due to the smaller detector capacitance, the amount of photons detected in each channel is lower, which means a lower slew rate, and therefore the benefit of segmenting is lost and CTR is not improved.

On the other side, the segmentation approach can benefit for this reduction in detector capacitance if an active summation scheme inside the ASIC is performed in order to recover the signal spread over the different channels and improve the Slew Rate due to segmentation and therefore improve the CTR.

We assume that a large sensor can be divided into m smaller detectors, which implies that

$$C_{large} = m \cdot C_{small} \tag{7}$$

in this situation, if series noise dominates, the total noise becomes proportional to $\sqrt{C}$ [22], which is the typical scenario for SiPMs with capacitances in the order of at least ten's of pF. Thus, the total noise of $\sigma_{n,large}$ becomes

$$\sigma_{n,large} \sim \sqrt{m} \cdot \sigma_{n,small} \tag{8}$$

then, if we sum m small detectors instead of the large one

$$\sigma_{n,m\cdot small} \sim \sqrt{m} \cdot \sigma_{n,small} \tag{9}$$

then, considering Eqs. (8) and (9)

$$\sigma_{n,large} \sim \sigma_{n,m\cdot small} \tag{10}$$

this means that the noise contribution of a large detector is approximately the same as the noise provided by the sum of m small detectors, assuming that series noise dominates and the impedance $Z_{DET} \gg Z_{in}$.

The peak voltage (amplitude) generated by the SIPM is directly related to the capacitance of the detector and increases approximately with C^{-1}. The response of the SiPM can be approximated as the sum of two exponential signals with time constants $\tau_{fast} = R_{load}C_{tot}$ and $\tau_{slow} = R_q(C_d + C_q)$ following the expression [25]

$$V(t) \sim \frac{QR_{load}}{C_d + C_q}\left(\frac{C_q}{\tau_{fast}}e^{\frac{-t}{\tau_{fast}}} + \frac{C_d}{\tau_{slow}}e^{\frac{-t}{\tau_{slow}}}\right) \tag{11}$$

where the total charge released in the cell is $Q = V_{ov}(C_d + C_q)$. This expression is valid for low input impedance FE electronics if that R_{load} is much smaller than the R_q [25]. The peak voltage is produced when the avalanche is quenched at instant$t = 0$ and thus

$$V_{peak} \sim R_{load}\left(\frac{Q_{fast}}{\tau_{fast}} + \frac{Q_{slow}}{\tau_{slow}}\right) \tag{12}$$

where the charge of the fast component is $Q_{fast} = Q\ C_q/(C_d + C_q)$ and the charge of the slow component is $Q_{slow} = Q\ C_d/(C_d + C_q)$. Eq. (12) shows that the peak voltage is produced by the slow component which depends mainly on the intrinsic parameters of the SiPM (R_q, C_d and C_q), which are independent on the total area or number of micro-cells of the SiPM and the fast component which is inversely proportional to C_{tot}^{-1}. Considering that the fast time constant is normally much smaller than the slow time constant and thus the charge produced by the fast component of the SiPM dominates, we can approximate the (V_{peak}) as:

$$V_{peak} \sim R_{load}\left(\frac{Q_{fast}}{\tau_{fast}}\right) \sim V_{ov}\left(\frac{C_q}{C_{tot}}\right) \tag{13}$$

Thus, we can conclude that the peak voltage is approximately inversely proportional to the overall capacitance of the cell and it is determined by the different number of micro-cells that forms the detector, i.e., the total capacitance. Then, considering the SiPM divided into m smaller detectors (same C_q but m times smaller C_{tot}), as detailed in Eq. (7), the peak voltage of an small detector would be

$$V_{peak,m\cdot small} \sim m \cdot V_{peak,large} \tag{14}$$

Therefore, a potential reduction of $t_{elec.}$ by a factor up to m ($m = 4$ for the case depicted in Fig. 11) can be achieved using the segmentation method approach. In practice, even if the series noise is dominating over the parallel noise, the reduction factor will be $m < 4$ as parallel noise is not negligible. It is important to highlight that this SPTR improvement requires a large bandwidth and low noise FE electronics to handle the fast response of the smaller sensor and not lose the benefit of segmentation.

4. Results on electronics jitter using segmentation

Using this new framework, we performed a transient noise simulation with Cadence Design using the test bench described in Fig. 11. The sigma from the electronics jitter (σ_{telec}) is obtained as the standard deviation of the arrival time of the first photon (photons are fired ideally at a given t0, but transient noise generates variations on the waveform, thus giving different arrival times as a result). The following simulations employ parts of the circuits of the HRFlexToT ASIC involved in the time response (pre-amplifier and discriminator) and a summation circuit based on a current mirror.

The FE parameters used in the following simulations are taken from the HRFlexToT ASIC.

Table 1
σ_{telec} comparison between different combinations of SiPMs with different detection areas. Micro-cell area of each sensor is the same.

SiPM ch. [mm^2]	1 × 1	3 × 3	1 × 1	3 × 3	3 × 3	6 × 6
num. of channels	9	1	18	2	4	1
det. area [mm^2]	9	9	18	18	36	36
σ_{telec} [ps]	79.1	92.9	100.1	139.2	224.3	378.7

Fig. 12 shows the σ_{telec} of the analog summation for different current thresholds at the comparator to determine the arrival time of the photon. In this particular simulation, the SiPM has a 50 μm × 50 μm cell size with intrinsic capacitance of 90 fF per cell and quenching resistance of 300 kΩ. Depending on the number of cells, the total capacitance of the devices varies between 36 pF and 324 pF for the 1 mm × 1 mm and 3 mm × 3 mm SiPM channel respectively, covering a total area of 3 mm × 3 mm. Note that the response of each SiPM has a different slew rate, noise figure and peak amplitude, hence changing the optimal threshold.

The framework is used to simulate larger detection areas involving a higher number of channels and adding the 6 mm × 6 mm SiPM sensor, with total capacitance of almost 1.3 nF. Table 1 illustrates the benefits of adding small SiPMs to cover a large detection area instead of using a large sensor with a larger capacitance. Small SiPMs present a larger peak amplitude and lower capacitance and therefore a better SNR. Moreover, they can benefit for its larger slew rate that provides a better time response. On the contrary, small SiPMs require a smart readout electronics to sum the signals from different SiPMs and thereby cover the same detection area of a large SiPM. This can lead to an increment on power consumption and complexity on the FE development.

From the above table we can see an improvement between 15% to 60%, depending on the detection area and segmentation, for the first photon time jitter. This results shows a solid prove of concept that the time resolution can be improved by using segmentation on large area SiPMs. Next section provides a detailed study on the impact of segmentation in the CTR.

5. Results on CTR using segmentation

A detailed study on CTR performance using the framework was done by simulating different SiPM sizes covering a given area. In the subsequent test cases, the electronics will be modeled using the equivalent FE circuit detailed in 8. The FE values regarding parallel and series noise are chosen based on the HRFlexToT performance, 10 $pA/\sqrt{Hz}$ and 1.5 $nV/\sqrt{Hz}$ respectively. Input resistance is set to 15 Ω and the bandwidth of the FE is set to 1 Ghz. The crystal is coupled to the SiPM using the thermoplastic Meltmount 1582 as optical coupler with a refraction index of 1.582. Lastly, we introduce a 0.1 mm dead spaces in all matrix distributions.

The first setup is composed by a LYSO crystal of 25 mm × 25 mm × 20 mm with all faces black painted except the one coupled to the photo-sensor. We evaluated four array configurations and their impact on timing performance. Different number of channels and same micro-cell size of 50 μm × 50 μm in all cases. In this case, only the FE electronics and an ideal leading-edge comparator has been used, i.e., analog summation is not applied, in order to be able to compare the simulation with experimental results using the 16 channels HRFlexToT ASIC (it does not have a summation circuit). In this case, the CTR is computed taking the pick up time from the fastest channel (see Table 2).

For the 6 mm × 6 mm SiPM size we have experimentally measured the CTR of the system using the 16 channels HRFlexToT readout. A CTR of 700 ps was obtained, indicating a small discrepancy with the simulation mainly due to the employment of the equivalent FE circuit. We can observe that the smaller the SiPM channel, the better the CTR value, except for the smallest one where the CTR shows a degradation. One possible reason for that could be an increment on

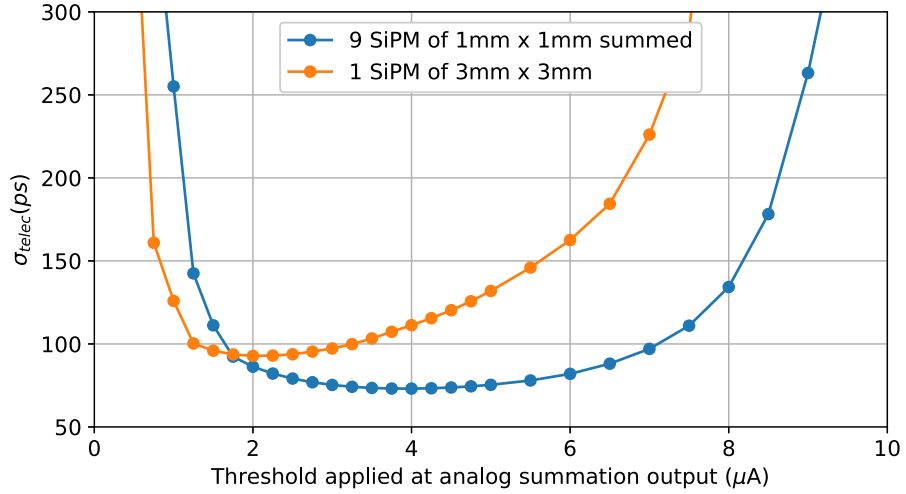

Fig. 12. Standard deviation comparison between single channel and segmentation. Total detection area equal to 9 mm^2.

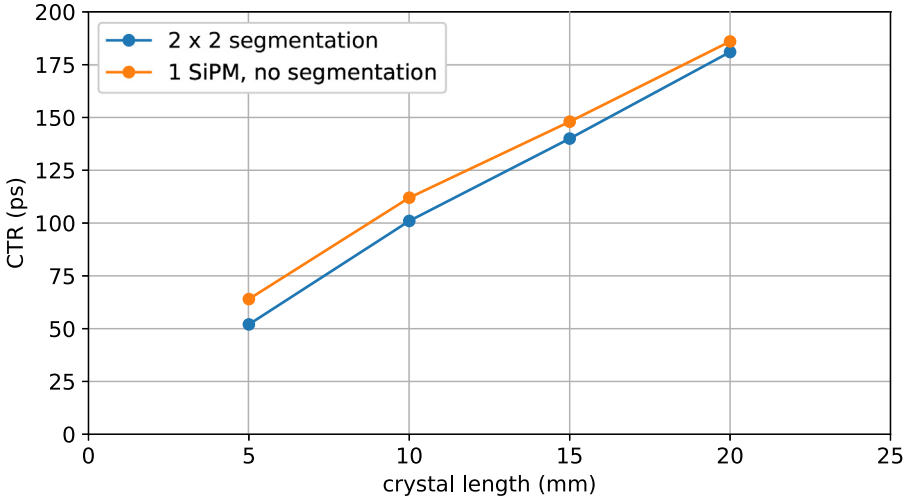

Fig. 13. Crystal length impact on the CTR performance plus comparison between 1 large SiPM (S14160-4050CS) and segmenting it into a 2 × 2 array.

Table 2
CTR simulation comparison between different combinations of SiPMs sizes with a 25 mm ×25 mm ×20 mm LYSO scintillator monolithic crystal.

SiPM ch. [mm^2]	1.5 × 1.5	2 × 2	3 × 3	6 × 6
num. of channels	256	144	64	16
det. area [mm^2]	625	625	625	625
CTR [ps]	430	419	465	642

the parallel noise, which implies that our previous hypothesis of series noise domination (detailed in 3) might not be longer valid. Another reason could be that the number of collected photons by a smaller detection area is lower and thus losing slew rate. This second reason implies that a summation scheme is needed to recover the signal (the collected photons) across several channels to avoid losing slew rate.

The next setup targets a better CTR using smaller crystals (less TTS) and teflon wrapping in order to collect as much light as possible during the photon-conversion. In ToF-PET scanners, one of the biggest contributions to the CTR worsening came from the scintillator crystal, as the travel time spread and the uncertainty on the depth of interaction for the gamma ray increases as a function of the crystal length. For this reason, this study case consists on a 4 mm × 4 mm × Z mm LYSO crystal teflon wrapped using Davis surface model coupled to a SiPM array of the same section and differently segmented. This Z variable corresponds to the length of the crystal and we simulated four different cases, 5 mm, 10 mm, 15 mm, and 20 mm.

A CTR study for all four crystal lengths and a S14160-4050CS SiPM without segmentation and dividing it in a 2 × 2 array, where all four outputs are summed and the single resulting output is calculated as depicted in Fig. 11. The final CTR plot versus the crystal length can be seen in Fig. 13. It shows the degradation of the CTR with respect to the crystal length and the improvement in terms of CTR by segmenting the sensor. Hence, a CTR below 100 ps would be only possible using LYSO crystals for lengths lower than 10 mm.

Table 3 shows more clearly how segmenting a large single SiPM can improve the CTR performance of the detector. We simulated three levels of segmentation: no-segmentation with a single SiPM of 4 mm × 4 mm. An array of 2 × 2 SiPMs of approximately 2 mm × 2 mm each. And a smaller channel of 1.3 mm × 1.3 mm in a 3 × 3 array distribution. The LYSO crystal size is set to 4 mm × 4 mm × 10 mm.

In this particular case, the CTR can be improved up to a 15% by implementing the segmentation technique. Observe that the intrinsic limit of the system is around 85 ps of CTR assuming perfect photon collection efficiency (PDE 100%) and no electronic noise, i.e., considering only the jitter from the optics (scintillator and SiPM). At a high segmentation value, the summation scheme allows for a further reduction in terms of CTR. Although, this improvement is becoming smaller due to fact that the parallel noise is starting to be more significant for lower

Table 3
Segmentation impact on CTR performance with a 10 mm long LYSO crystal and different segmentation factor of a S14160-4050CS SiPM. Ideal sensor corresponds to 100% on PDE, considering only the jitter from the optics (scintillator and SiPM SPTR).

SiPM ch. [mm^2]	4 × 4	2 × 2	1.3 × 1.3	Ideal
num. of channels	1	4	9	1
det. area [mm^2]	4	4	4	4
CTR [ps]	112	101	97	85

capacitances of the sensor [22]. At this point, further studies of the FE parameters considering also bandwidth, power consumption, larger segmentation and the implementation of the FE electronics at transistor level with different topologies are planned for the near future.

6. Conclusions and future research

We provide a new design framework that will enable a global optimization of the PET system that considers the scintillator, the sensor (sensor size, pixel pitch, dead area, capacitance) and the readout electronics (input impedance, noise, bandwidth, summation). This framework gives the possibility to choose the best sensor considering both the light generation and transport employing GATE and the readout response using an electrical simulator. Furthermore, the framework enables a comprehensive optimization of sensor and front end, considering a segmentation of the sensor which allows potential optimization of the overall CTR.

Simulation results showed that the segmentation technique might allow a potential reduction of the CTR achieving resolutions at the order of 100 ps with small crystals. Although, it is clear that to go below 50 ps new scintillators coupled to fast efficient electronics will be mandatory. Future work will include the implementation of uncorrelated (DCR) and correlated (after-pulsing and cross-talk) noise at the sensor level. Implementation of efficient FE electronics at transistor level applying the segmentation technique. Moreover, exploration of new geometries and scintillator materials are planned. All this new features, will studied using the here presented simulation framework.

CRediT authorship contribution statement

David Sánchez: Writing - review & editing, Visualization, Software, Investigation. **Sergio Gómez:** Supervision, Investigation. **José María Fernández-Tenllado:** Formal analysis, Methodology. **Rafael Ballabriga:** Funding acquisition, Methodology. **Michael Campbell:** Project administration. **David Gascón:** Supervision, Conceptualization.

Declaration of competing interest

The authors declare that they have no known competing financial interests or personal relationships that could have appeared to influence the work reported in this paper.

Acknowledgments

This work has been supported by the ATTRACT project funded by the European Comission under Grant Agreement 777222, the CERN KT fund, and by the ERDF under the Spanish MINECO (FPA2016-80917-R).

References

[1] E. Garutti, Silicon photomultipliers for high energy physics detectors, J. Instrum. 6 (10) (2011) http://dx.doi.org/10.1088/1748-0221/6/10/C10003, arXiv:1108.3166.

[2] N. Otte, B. Dolgoshein, J. Hose, S. Klemin, E. Lorenz, R. Mirzoyan, E. Popova, M. Teshima, The potential of SiPM as photon detector in astroparticle physics experiments like MAGIC and EUSO, Nuclear Phys. B Proc. Suppl. 150 (1–3) (2006) 144–149, http://dx.doi.org/10.1016/j.nuclphysbps.2004.10.084.

[3] H. Miyamoto, M. Teshima, SiPM development for the imaging Cherenkov and fluorescence telescopes, Nucl. Instrum. Methods Phys. Res. A 623 (1) (2010) 198–200, http://dx.doi.org/10.1016/j.nima.2010.02.194, http://dx.doi.org/10.1016/j.nima.2010.02.194.

[4] S. Korpar, R. Dolenec, P. Križan, R. Pestotnik, A. Stanovnik, Study of TOF PET using Cherenkov light, Nucl. Instrum. Methods Phys. Res. A 654 (1) (2011) 532–538, http://dx.doi.org/10.1016/j.nima.2011.06.035.

[5] A.T. Fienberg, L.P. Alonzi, A. Anastasi, R. Bjorkquist, D. Cauz, R. Fatemi, C. Ferrari, A. Fioretti, A. Fankenthal, C. Gabbanini, L.K. Gibbons, K. Giovanetti, S.D. Goadhouse, W.P. Gohn, T.P. Gorringe, D.W. Hertzog, M. Iacovacci, P. Kammel, J. Kaspar, B. Kiburg, L. Li, S. Mastroianni, G. Pauletta, D.A. Peterson, D. Počanić, M.W. Smith, D.A. Sweigart, V. Tishchenko, G. Venanzoni, T.D. Van Wechel, K.B. Wall, P. Winter, K. Yai, Studies of an array of PbF2 Cherenkov crystals with large-area SiPM readout, Nucl. Instrum. Methods Phys. Res. A 783 (2015) 12–21, http://dx.doi.org/10.1016/j.nima.2015.02.028.

[6] C. Perrina, The future of the high energy cosmic ray detection: HERD, EPJ Web Conf. 209 (201 9) (2019) 01040, http://dx.doi.org/10.1051/epjconf/201920901040.

[7] R. Agishev, A. Comerón, J. Bach, A. Rodriguez, M. Sicard, J. Riu, S. Royo, Lidar with SiPM: Some capabilities and limitations in real environment, Opt. Laser Technol. 49 (2013) 86–90, http://dx.doi.org/10.1016/j.optlastec.2012.12.024.

[8] G. Adamo, A. Busacca, Time Of Flight measurements via two LiDAR systems with SiPM and APD, in: AEIT 2016 - International Annual Conference: Sustainable Development in the Mediterranean Area, Energy and ICT Networks of the Future, AEIT, 2016, http://dx.doi.org/10.23919/AEIT.2016.7892802.

[9] T. Jones, D. Townsend, History and future technical innovation in positron emission tomography, J. Med. Imaging 4 (1) (2017) 011013, http://dx.doi.org/10.1117/1.jmi.4.1.011013.

[10] S. Surti, Update on time-of-flight PET imaging, J. Nucl. Med. 56 (1) (2015) 98–105, http://dx.doi.org/10.2967/jnumed.114.145029.

[11] J. Van Sluis, J. De Jong, J. Schaar, W. Noordzij, P. Van Snick, R. Dierckx, R. Borra, A. Willemsen, R. Boellaard, Performance characteristics of the digital biograph vision PET/CT system, J. Nucl. Med. 60 (7) (2019) 1031–1036, http://dx.doi.org/10.2967/jnumed.118.215418.

[12] R.D. Badawi, H. Shi, P. Hu, S. Chen, T. Xu, P.M. Price, Y. Ding, B.A. Spencer, L. Nardo, W. Liu, J. Bao, T. Jones, H. Li, S.R. Cherry, First human imaging studies with the explorer total-body PET scanner, J. Nucl. Med. 60 (3) (2019) 299–303, http://dx.doi.org/10.2967/jnumed.119.226498.

[13] S. Gundacker, E. Auffray, K. Pauwels, P. Lecoq, Measurement of intrinsic rise times for various L(Y)SO and LuAG scintillators with a general study of prompt photons to achieve 10 ps in TOF-PET, Phys. Med. Biol. 61 (7) (2016) 2802–2837, http://dx.doi.org/10.1088/0031-9155/61/7/2802.

[14] J.J. Vaquero, P. Kinahan, Positron emission tomography: Current challenges and opportunities for technological advances in clinical and preclinical imaging systems, Annu. Rev. Biomed. Eng. 17 (2015) 385–414, http://dx.doi.org/10.1146/annurev-bioeng-071114-040723.

[15] P. Lecoq, Pushing the limits in time-of-flight PET imaging, IEEE Trans. Radiat. Plasma Med. Sci. 1 (6) (2017) 473–485, http://dx.doi.org/10.1109/TRPMS.2017.2756674, http://ieeexplore.ieee.org/document/8049484/.

[16] M.V. Nemallapudi, S. Gundacker, P. Lecoq, E. Auffray, Single photon time resolution of state of the art SiPMs, J. Instrum. 11 (10) (2016) http://dx.doi.org/10.1088/1748-0221/11/10/P10016.

[17] N. Dinu, Z. Amara, C. Bazin, V. Chaumat, C. Cheikali, G. Guilhem, V. Puill, C. Sylvia, J.F. Vagnucci, Electro-optical characterization of SiPM: A comparative study, Nucl. Instrum. Methods Phys. Res. A 610 (1) (2009) 423–426, http://dx.doi.org/10.1016/j.nima.2009.05.101, http://dx.doi.org/10.1016/j.nima.2009.05.101.

[18] S. Gundacker, R. Martinez Turtos, N. Kratochwil, R.H. Pots, M. Paganoni, P. Lecoq, E. Auffray, Experimental time resolution limits of modern SiPMs and TOF-PET detectors exploring different scintillators and Cherenkov emission, Phys. Med. Biol. 65 (2) (2020) http://dx.doi.org/10.1088/1361-6560/ab63b4.

[19] Cadence Design Systems, Inc., https://www.cadence.com.

[20] S. Jan, G. Santin, D. Strul, S. Staelens, K. Assié, D. Autret, S. Avner, R. Barbier, M. Bardiès, P.M. Bloomfield, D. Brasse, V. Breton, P. Bruyndonckx, I. Buvat, A.F. Chatziioannou, Y. Choi, Y.H. Chung, C. Comtat, D. Donnarieix, L. Ferrer, S.J. Glick, C.J. Groiselle, D. Guez, P.F. Honore, S. Kerhoas-Cavata, A.S. Kirov, V. Kohli, M. Koole, M. Krieguer, D.J. van der Laan, F. Lamare, G. Largeron, C. Lartizien, D. Lazaro, M.C. Maas, L. Maigne, F. Mayet, F. Melot, C. Merheb, E. Pennacchio, J. Perez, U. Pietrzyk, F.R. Rannou, M. Rey, D.R. Schaart, C.R. Schmidtlein, L. Simon, T.Y. Song, J.M. Vieira, D. Visvikis, R. Van de Walle, E. Wieërs, C. Morel, GATE: A simulation toolkit for PET and SPECT, Phys. Med. Biol. 49 (19) (2004) 4543–4561, http://dx.doi.org/10.1088/0031-9155/49/19/007, arXiv:0408109.

[21] M. Stockhoff, S. Jan, A. Dubois, S.R. Cherry, E. Roncali, Advanced optical simulation of scintillation detectors in GATE V8.0: First implementation of a reflectance model based on measured data, Phys. Med. Biol. 62 (12) (2017) L1–L8, http://dx.doi.org/10.1088/1361-6560/aa7007.

[22] J.M. Fernandez-Tenllado, R. Ballabriga, M. Campbell, D. Gascon, S. Gomez, J. Mauricio, Optimal design of single-photon sensor front-end electronics for fast-timing applications, in: 2019 IEEE Nuclear Science Symposium and Medical Imaging Conference, NSS/MIC 2019, http://dx.doi.org/10.1109/NSS/MIC42101.2019.9059805.

[23] S. Seifert, H.T. Van Dam, J. Huizenga, R. Vinke, P. Dendooven, H. Löhner, D.R. Schaart, Simulation of silicon photomultiplier signals, IEEE Trans. Nucl. Sci. 56 (6) (2009) 3726–3733, http://dx.doi.org/10.1109/TNS.2009.2030728.

[24] F. Acerbi, S. Gundacker, Understanding and simulating SiPMs, Nucl. Instrum. Methods Phys. Res. A 926 (September 2018) (2019) 16–35, http://dx.doi.org/10.1016/j.nima.2018.11.118, https://doi.org/10.1016/j.nima.2018.11.118.

[25] G. Collazuol, The SiPM Physics and Technology - a Review, PhotoDet 2012, (June) 2012, p. 74, http://indico.cern.ch/event/164917/contribution/72/material/slides/0.pdf.

[26] A. Sanuy, D. Gascon, M. Paredes, L. Garrido, M. Ribó, J. Sieiro, Wideband (500 MHz) 16 bit dynamic range current mode PreAmplifier for the CTA cameras (PACTA), J. Instrum. 7 (1) (2012) http://dx.doi.org/10.1088/1748-0221/7/01/C01100.

[27] N. Dinu, Instrumentation on silicon detectors: from properties characterization to applications, Université Paris Sud - Paris XI, 2013, https://tel.archives-ouvertes.fr/tel-00872318.

[28] T. Noulis, CMOS process transient noise simulation analysis and benchmarking, in: Proceedings - 2016 26th International Workshop on Power and Timing Modeling, Optimization and Simulation, PATMOS 2016, IEEE, 2017, pp. 70–75, http://dx.doi.org/10.1109/PATMOS.2016.7833428.

[29] S. Gomez, D. Sanchez, D. Gascon, J.M. Cela, L. Freixas, R. Graciani, R. Manera, J. Marin, J. Mauricio, J.J. Navarrete, J.C. Oller, J.M. Perez, P. Rato Mendes, A. Sanmukh, O. Vela, A High Dynamic Range ASIC for Time of Flight PET with pixelated and monolithic crystals, in: 2019 IEEE Nuclear Science Symposium and Medical Imaging Conference, NSS/MIC 2019, (September) 2019, pp. 17–21, http://dx.doi.org/10.1109/NSS/MIC42101.2019.9059762.

[30] F. Corsi, C. Marzocca, A. Perrotta, A. Dragone, M. Foresta, A. Del Guerra, S. Marcatili, G. Llosa, G. Collazzuol, G.F. Dalla Betta, N. Dinu, C. Piemonte, G.U. Pignatel, G. Levi, Electrical characterization of silicon photo-multiplier detectors for optimal front-end design, in: IEEE Nuclear Science Symposium Conference Record, 2, IEEE, 2006, pp. 1276–1280, http://dx.doi.org/10.1109/NSSMIC.2006.356076.

[31] P. Buzhan, B. Dolgoshein, L. Filatov, A. Ilyin, V. Kaplin, A. Karakash, S. Klemin, R. Mirzoyan, A.N. Otte, E. Popova, V. Sosnovtsev, M. Teshima, Large area silicon photomultipliers: Performance and applications, Nucl. Instrum. Methods Phys. Res. A 567 (1 SPEC. ISS.) (2006) 78–82, http://dx.doi.org/10.1016/j.nima.2006.05.072.

[32] S.M. Decker, M. Pizzichemi, A. Polesel, M. Paganoni, E. Auffray, S. Gundacker, The digital-analog SiPM approach: A story of electronic and excess noise, in: 2019 IEEE Nuclear Science Symposium and Medical Imaging Conference, NSS/MIC 2019, IEEE, 2019, http://dx.doi.org/10.1109/NSS/MIC42101.2019.9059792.

[33] F. Anghinolfi, P. Jarron, A.N. Martemiyanov, E. Usenko, H. Wenninger, M.C.S. Williams, A. Zichichid, NINO: an ultra-fast and low-power front-end amplifier/discriminator ASIC designed for the multigap resistive plate chamber, Nucl. Instrum. Methods Phys. Res. A 533 (2004) https://doi.org/10.1016/j.nima.2004.07.024.